Accepted Manuscript

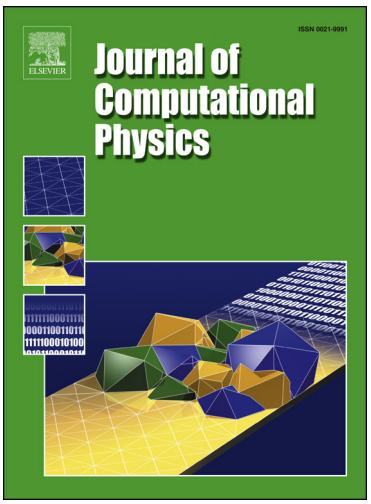

The PAC-MAN model: Benchmark case for linear acoustics in computational physics

Harald Ziegelwanger, Paul Reiter

PII: S0021-9991(17)30463-1
DOI: http://dx.doi.org/10.1016/j.jcp.2017.06.018
Reference: YJCPH 7417

To appear in: *Journal of Computational Physics*

Received date: 17 March 2017
Revised date: 6 June 2017
Accepted date: 7 June 2017

Please cite this article in press as: H. Ziegelwanger, P. Reiter, The PAC-MAN model: Benchmark case for linear acoustics in computational physics, *J. Comput. Phys.* (2017), http://dx.doi.org/10.1016/j.jcp.2017.06.018

Highlights

- A benchmark case for 2D harmonic linear acoustic problems is proposed.
- The PAC-MAN geometry is used as emitter/scatterer in this benchmark.
- An analytic formulation of radiated and scattered sound is derived.
- Line and disk sources, plane waves, and surface vibrations are considered.

The PAC-MAN Model: Benchmark Case for Linear Acoustics in Computational Physics

Harald Ziegelwanger[a,*], Paul Reiter[a,b]

[a] *AIT Austrian Institute of Technology GmbH, Center for Mobility Systems, Giefinggasse 2, 1210 Vienna, Austria*
[b] *TU Wien, Institute of Applied Physics, Wiedner Hauptstr. 8-10/134, 1040 Vienna, Austria*

Abstract

Benchmark cases in the field of computational physics, on the one hand, have to contain a certain complexity to test numerical edge cases and, on the other hand, require the existence of an analytical solution, because an analytical solution allows the exact quantification of the accuracy of a numerical simulation method. This dilemma causes a need for analytical sound field formulations of complex acoustic problems. A well known example for such a benchmark case for harmonic linear acoustics is the "Cat's Eye model", which describes the three-dimensional sound field radiated from a sphere with a missing octant analytically. In this paper, a benchmark case for two-dimensional (2D) harmonic linear acoustic problems, viz., the "PAC-MAN model", is proposed. The PAC-MAN model describes the radiated and scattered sound field around an infinitely long cylinder with a cut out sector of variable angular width. While the analytical calculation of the 2D sound field allows different angular cut-out widths and arbitrarily positioned line sources, the computational cost associated with the solution of this problem is similar to a 1D problem because of a modal formulation of the sound field in the PAC-MAN model.

Keywords: Computational Acoustics, Benchmarks, Harmonic Linear Acoustics, Mode coupling, Sound Radiation, Sound Scattering
PACS: 43.20.Fn, 43.20.Ks, 43.20.Rz

1. Introduction

In the field of computational acoustics benchmark cases are required for the evaluation and verification of numerical simulation methods (Hornikx et al., 2015). Usually simple acoustic problems, i.e., problems for which an analytical solution is known, are used as benchmark in the literature, e.g., the sound field of a point source scattered by a rigid sphere was used in Ziegelwanger et al. (2015), the sound field of a point source scattered by an infinite rigid cylinder Tam and Hardin (1997) was used in Duhamel (1996) and Kasess et al. (2016), or the sound field in a rigid duct was used in Marburg (2002). Benchmark cases, however, should contain a certain complexity to test numerical edge cases (Simpson and Landman, 2007; Le Bars and Worster, 2006), e.g., corners in the geometry of a scatterer – problems where an analytical solution of the sound field is usually not known. An analytic solution, however, is essential for the exact quantification of the accuracy of a numerical procedure. This dilemma causes a need for analytical solutions of complex acoustic problems. A well known example for a complex three-dimensional (3D) benchmark case is the "Cat's Eye Model" (Mechel, 2005). The cat's eye geometry is a sphere with a missing octant and, thus, includes a corner at the center of the sphere and sharp edges. The cat's eye *model* analytically describes the sound field generated by a surface velocity distribution on the cat's eye surface.

*Corresponding Author: +43 50550-6611
Email addresses: harald.ziegelwanger@ait.ac.at (Harald Ziegelwanger), paul.reiter.fl@ait.ac.at (Paul Reiter)

In this paper, a benchmark case for two-dimensional (2D) harmonic linear acoustics is proposed, which is the 2D equivalent to the 3D cat's eye model. The name of the proposed model originates from its geometry, i.e., a circle with a cut out sector of variable angular width, which resembles the shape of a popular computer game character of the 1980s (Melissinos et al., 2012; Loguidice and Barton, 2009), viz., the PAC-MAN. Figure 1 illustrates the PAC-MAN model. A sector of a circle (representing an infinitely long cylinder of radius r_0) is cut out; the side edges of the cut-out (at $\varphi = \pm\varphi_0$) are assumed to be rigid. The PAC-MAN shape was observed and investigated in other research fields, e.g., in solar system studies (Howett et al., 2012) and in magnetism (Cambel et al., 2013), respectively.

To retrieve an analytical solution of the sound field around the PAC-MAN, the exterior domain was separated into two zones, viz., zone (I) outside the cylinder, and zone (II) in the cut out sector. The analytic solution was found by coupling the modes of zone (I) and zone (II) for the defined boundary conditions and the defined excitation of the acoustic system. The proposed analytical solution is able to describe various excitation patterns of the acoustic system. First, the radiation of surface vibrations in which the surface of the PAC-MAN oscillates with cylindrical modes can be calculated. Second, equations to describe the scattering of cylindrical waves emitted by an arbitrarily positioned line source were derived, which result in an analytical and semi-analytical calculation for source positions in (I) and (II), respectively. While line sources can be easily implemented in a boundary element code, they cause problems in finite element codes, e.g., computational aeroacoustics, due to the logarithmic singularity at the source position (Morris, 1995). Thus, third, the excitation by a spatially distributed cylindrical source was considered which can be implemented in both boundary element and finite element codes. Fourth, the scattering of plane waves with arbitrary angle of incidence were developed. Finally, all excitation patterns were tested in numerical examples, where the cut-out width in the PAC-MAN model was varied and the calculated sound field was compared to the sound field radiated and scattered by a simple cylinder.

2. Sound field formulation

The sound field is formulated in a polar co-ordinate system r, φ, where the coordinate axis $\varphi = 0$ is in the middle of (II). The 2D sound pressure field p is described by the 2D Helmholtz-Equation in polar coordinates (Beranek and Mellow, 2012):

$$\frac{1}{r}\frac{\partial}{\partial r}\left(r\frac{\partial p(r,\varphi)}{\partial r}\right) + \frac{1}{r^2}\frac{\partial^2 p(r,\varphi)}{\partial \varphi^2} + k^2 p(r,\varphi) = 0, \tag{1}$$

and the particle velocity $\mathbf{v}$ of the sound pressure field is given by:

$$\mathbf{v} = \frac{\mathrm{i}}{kZ_0}\mathrm{grad}p, v_r = \frac{\mathrm{i}}{kZ_0}\frac{\partial p}{\partial r}, v_\varphi = \frac{\mathrm{i}}{kZ_0}\frac{\partial p}{r\partial \varphi}, \tag{2}$$

where for simplification the time factor $e^{\mathrm{i}\omega t}$ is dropped, $k = \frac{\omega}{c_0}$ and $Z_0 = \rho_0 c_0$ are the wave number and the characteristic field impedance, with ρ_0 the density of the medium and c_0 the speed of sound in the medium. The solution of the sound pressure field $p(r, \varphi)$ separates into:

$$p(r,\varphi) = R(kr)\Phi(\varphi). \tag{3}$$

where

$$R(kr) = A_\nu^{(1)}\mathcal{R}_\nu^{(1)}(kr) + A_\nu^{(2)}\mathcal{R}_\nu^{(2)}(kr) \tag{4}$$

is the radial part with $A_\nu^{(1)}$ and $A_\nu^{(2)}$ the radial mode amplitudes, ν the mode order, and $\mathcal{R}_\nu^{(1)}(kr)$ and $\mathcal{R}_\nu^{(2)}(kr)$ the independent Bessel functions, i.e., either a superposition of Bessel functions of the first and second kind, or a superposition of Hankel functions of the first and second kind, respectively. The former is a superposition of real-valued standing waves with and without phase jump at the origin, the latter is a superposition of complex-valued incoming and outgoing waves.

$$\Phi(\varphi) = A_\nu^{\mathcal{A}}\sin(\nu\varphi) + A_\nu^{\mathcal{S}}\cos(\nu\varphi) \tag{5}$$

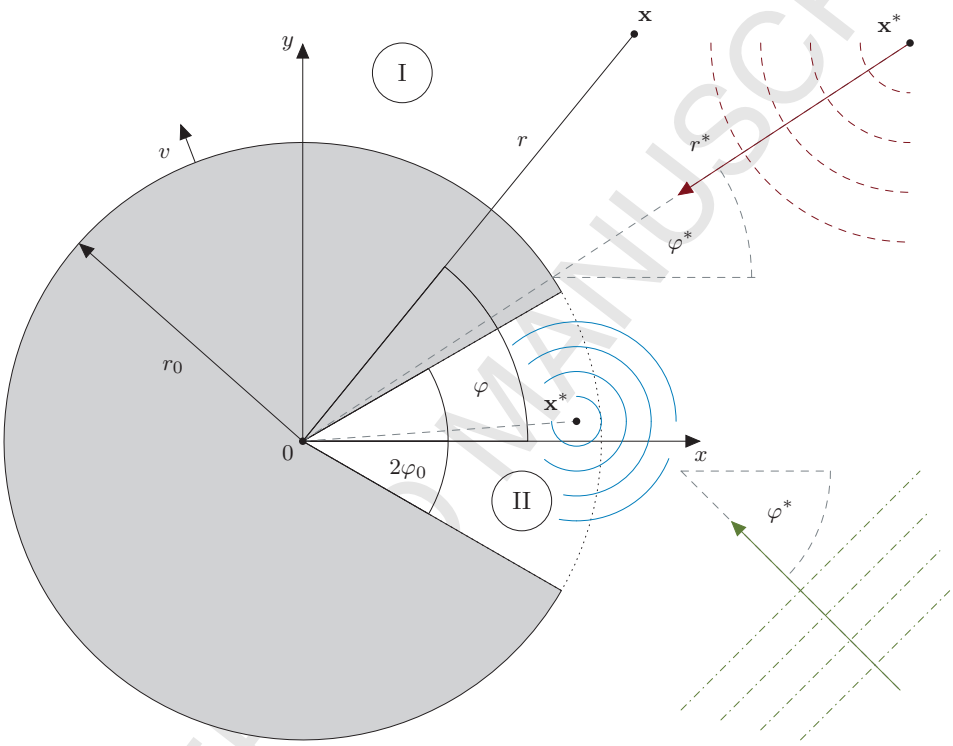

Figure 1: The PAC-MAN model consists of a circle (radius r_0) with a circular sector of angular width $2\varphi_0$ cut out. Incident sound field is schematically shown for a cylindrical wave originating from the exterior zone (- - -), a cylindrical wave originating from the interior zone (——), and a plane wave (-·-·-). $\mathbf{x}^*$ is the source position of a cylindrical wave described by its distance r^* and angle φ^*. v is the velocity of a surface vibration.

is the angular part with $A_\nu^{\mathcal{A}}$and $A_\nu^{\mathcal{S}}$ the angular mode amplitudes of the anti-symmetric and symmetric part, respectively.

In the *exterior zone* (I), $\mathcal{R}_\nu^{(2)}(kr)$ has to be the Hankel function of second kind $H_\nu^{(2)}(kr)$ to comply with Sommerfeld's radiation condition and $\mathcal{R}_\nu^{(1)}$ has to be zero (Beranek and Mellow, 2012). The continuity of the sound pressure demands a periodicity of the field in φ on orbits around the cylinder, thus, $\nu = n = 0, 1, 2, \ldots$ have to be integer numbers (Williams, 1999). The field in (I) can be formulated as an infinite sum of symmetric and anti-symmetric modes:

$$p^{(I)}(r,\varphi) = \sum_{n=0}^{\infty} \left\{ a_n^{\mathcal{A}} H_n^{(2)}(kr) \sin(n\varphi) + a_n^{\mathcal{S}} H_n^{(2)}(kr) \cos(n\varphi) \right\} \tag{6}$$

$$Z_0 v_r^{(I)}(r,\varphi) = \mathrm{i} \sum_{n=0}^{\infty} \left\{ a_n^{\mathcal{A}} H_n'^{(2)}(kr) \sin(n\varphi) + a_n^{\mathcal{S}} H_n'^{(2)}(kr) \cos(n\varphi) \right\} \tag{7}$$

where $a_n^{\mathcal{A}} = A_\nu^{(2)} A_\nu^{\mathcal{A}}$ and $a_n^{\mathcal{S}} = A_\nu^{(2)} A_\nu^{\mathcal{S}}$ are the anti-symmetric and symmetric mode amplitudes in the exterior zone, respectively. A prime indicates the derivative with respect to the argument.

For the *interior zone* (II), the regularity at $r = 0$ demands $\mathcal{R}_\nu^{(1)}(kr) = J_\nu(kr)$ and $\mathcal{R}_\nu^{(2)}$ has to be zero (Beranek and Mellow, 2012). Since the edges of the cut-out sector in the PAC-MAN model are defined to be rigid, the condition $v_\varphi \xrightarrow[\varphi \to \pm\varphi_0]{} 0$ has to be fulfilled. For all possible mode orders of the anti-symmetric part $\nu_{\mathcal{A}}$ and the symmetric part $\nu_{\mathcal{S}}$, this implies

$$\begin{aligned} A_{\nu_{\mathcal{A}}}^{\mathcal{A}} \cos(\nu_{\mathcal{A}}\varphi_0) - A_{\nu_{\mathcal{S}}}^{\mathcal{S}} \sin(\nu_{\mathcal{S}}\varphi_0) &\overset{!}{=} 0, \\ A_{\nu_{\mathcal{A}}}^{\mathcal{A}} \cos(-\nu_{\mathcal{A}}\varphi_0) - A_{\nu_{\mathcal{S}}}^{\mathcal{S}} \sin(-\nu_{\mathcal{S}}\varphi_0) &\overset{!}{=} 0, \\ \cos(\nu_{\mathcal{A}}\varphi_0) \overset{!}{=} 0 \Rightarrow \nu_{\mathcal{A}}\varphi_0 &= \pi\left(\eta + \frac{1}{2}\right), \end{aligned} \tag{8}$$

$$\sin(\nu_{\mathcal{S}}\varphi_0) \overset{!}{=} \sin(-\nu_{\mathcal{S}}\varphi_0) \Rightarrow \nu_{\mathcal{S}}\varphi_0 = \pi\eta, \tag{9}$$

where $\eta = 0, 1, 2, \ldots$ are integer numbers. As in Mechel (2005), the further analysis is simplified by restricting φ_0 to integer fractions of π:

$$\varphi_0 = \pi/N: \qquad N = 2, 3, 4, \ldots \tag{10}$$

so that the mode orders $\nu_{\mathcal{A}}$ and $\nu_{\mathcal{S}}$ become integer numbers:

$$\nu_{\mathcal{A}} = \left(\eta + \frac{1}{2}\right) N, \tag{11}$$

$$\nu_{\mathcal{S}} = \eta N. \tag{12}$$

The sound field formulation in (II) satisfying the conditions of regularity and the boundary conditions at the rigid edges of the cut-out results in:

$$p^{(II)}(r,\varphi) = \sum_{\eta=0}^{\infty} \left\{ b_{(\eta+\frac{1}{2})N}^{\mathcal{A}} J_{(\eta+\frac{1}{2})N}(kr) \sin\left(\left(\eta + \frac{1}{2}\right) N\varphi\right) + b_{\eta N}^{\mathcal{S}} J_{\eta N}(kr) \cos(\eta N\varphi) \right\} \tag{13}$$

$$Z_0 v_r^{(II)}(r,\varphi) = \mathrm{i} \sum_{\eta=0}^{\infty} \left\{ b_{(\eta+\frac{1}{2})N}^{\mathcal{A}} J'_{(\eta+\frac{1}{2})N}(kr) \sin\left(\left(\eta + \frac{1}{2}\right) N\varphi\right) + b_{\eta N}^{\mathcal{S}} J'_{\eta N}(kr) \cos(\eta N\varphi) \right\} \tag{14}$$

where $b_{(\eta+\frac{1}{2})N}^{\mathcal{A}} = A_{\nu=(\eta+\frac{1}{2})N}^{(1)} A_{\nu=(\eta+\frac{1}{2})N}^{\mathcal{A}}$ and $b_{\eta N}^{\mathcal{S}} = A_{\nu=\eta N}^{(1)} A_{\nu=\eta N}^{\mathcal{S}}$ are the anti-symmetric and symmetric mode amplitudes in the interior zone, respectively. Orthogonality of the modes is shown in Appendix A.

3. Excitation of the acoustic system

3.1. Surface vibrations

The excitation on the outer surface of the PAC-MAN geometry can be determined by particle velocity mode amplitudes V_{n*}^{vib}:

$$Z_0 v_{vib}(r_0,\varphi) = \sum_{n^*=0}^{\infty} Z_0 V_{n^*}^{\mathcal{A},vib} \sin(n^*\varphi) + \sum_{n^*=0}^{\infty} Z_0 V_{n^*}^{\mathcal{S},vib} \cos(n^*\varphi) \qquad \texttt{for} \quad \varphi = (\varphi_0, 2\pi-\varphi_0)\,, \tag{15}$$

where v_{vib} is the radial surface particle velocity and n^* is the order of the vibration modes. The particle velocity mode amplitudes are related with the sound pressure amplitudes $P_{n^*}^{vib}$ by

$$V_{n^*}^{vib} = \mathrm{i}\frac{H_{n^*}^{'(2)}(kr_o)}{Z_0 H_{n^*}^{(2)}(kr_0)} P_{n^*}^{vib}. \tag{16}$$

3.2. Line source in the exterior zone

With Graf's addition theorem for Bessel functions (Abramowitz and Stegun, 1964) the sound field generated by a line source located in the exterior domain can be calculated by an infinite mode sum (Cavicchi and O'Brien, 1988). Then, the incident sound pressure is calculated by:

$$\begin{aligned} p_{inc}^{(I)}(r,\varphi) =& \sum_{n^*=0}^{\infty} \underbrace{\delta_{n^*} J_{n^*}(kr) H_{n^*}^{(2)}(kr^*)}_{P_{n^*}^{inc}(kr)} \cos\left(n^*\left(\varphi-\varphi^*\right)\right) \\ =& \sum_{n^*=0}^{\infty} P_{n^*}^{inc}(kr) \sin\left(n^*\varphi^*\right) \sin\left(n^*\varphi\right) + \sum_{n^*=0}^{\infty} P_{n^*}^{inc}(kr) \cos\left(n^*\varphi^*\right) \cos\left(n^*\varphi\right), \end{aligned} \tag{17}$$

and the incident particle velocity by:

$$\begin{aligned} Z_0 v_{r,inc}^{(I)}(r,\varphi) =& \mathrm{i}\sum_{n^*=0}^{\infty} \underbrace{\delta_{n^*} J'_{n^*}(kr) H_{n^*}^{(2)}(kr^*)}_{V_{n^*}^{inc}(kr)} \cos\left(n^*\left(\varphi-\varphi^*\right)\right) \\ =& \mathrm{i}\sum_{n^*=0}^{\infty} V_{n^*}^{inc}(kr) \sin\left(n^*\varphi^*\right) \sin\left(n^*\varphi\right) + \mathrm{i}\sum_{n^*=0}^{\infty} V_{n^*}^{inc}(kr) \cos\left(n^*\varphi^*\right) \cos\left(n^*\varphi\right), \end{aligned} \tag{18}$$

where δ_{n^*} is the Heaviside symbol and r^* and φ^* are the polar coordinates of the line source.

3.3. Line source in the interior zone

Since Graf's addition theorem for Bessel function does not hold for $r^* \leq r_0$, the sound field generated by a line source located in zone (II) can not be calculated directly by an infinite mode sum. But the modes of the sound field in zone (II) can be calculated indirectly in three steps. First, N rotational mirror sources are placed inside the PAC-MAN to comply with the boundary condition of rigid edges of the cut-out, where the position of the m-th mirror source is given by $\varphi_m^* = 2\varphi_0 m + (-1)^m \varphi^*$. Note that this mirror source technique further restricts N to *even* integer numbers only. Second, the pressure sound field $p(r_0,\varphi)$ for the superposed mirror sources is evaluated at a finite set of points at the interface between (I) and (II), where φ is uniformly distributed between $-\varphi_0$ and φ_0. Finally, the mode amplitudes of $p(\mathbf{x})$ are calculated by solving a linear system of equations

$$\frac{p(r_0,\varphi)-p(r_0,-\varphi)}{2} = \sum_{n^*=0}^{\infty} \underbrace{c_{n^*}^{\mathcal{A}} H_{(n^*+\frac{1}{2})N}^{(2)}(kr_0)}_{P_{n^*}^{\mathcal{A},inc}(kr_0)} \sin\left(\left(n^*+\frac{1}{2}\right)N\varphi\right) \tag{19}$$

for the anti-symmetric part of $p(r_0,\varphi)$ and

$$\frac{p(r_0,\varphi)+p(r_0,-\varphi)}{2}=\sum_{n^*=0}^{\infty}\underbrace{c_{n^*}^{\mathcal{S}}H_{n^*N}^{(2)}(kr_0)}_{P_{n^*}^{\mathcal{S},inc}(kr_0)}\cos\left(n^*N\varphi\right) \tag{20}$$

for the symmetric part of $p(r_0,\varphi)$.

Finally, the incident pressure sound field at r_0 is calculated by

$$p_{inc}^{(II)}(r_0,\varphi)=\sum_{n^*=0}^{\infty}P_{n^*}^{\mathcal{A},inc}(kr_0)\sin\left(\left(n^*+\frac{1}{2}\right)N\varphi\right)+\sum_{n^*=0}^{\infty}P_{n^*}^{\mathcal{S},inc}(kr_0)\cos\left(n^*N\varphi\right), \tag{21}$$

and, consequently, the incident particle velocity sound field at r_0 is calculated by

$$Z_0v_{r,inc}^{(II)}(r_0,\varphi)=\mathrm{i}\sum_{n^*=0}^{\infty}\underbrace{c_{n^*}^{\mathcal{A}}H_{(n^*+\frac{1}{2})N}^{'(2)}(kr_0)}_{V_{n^*}^{\mathcal{A},inc}(kr_0)}\sin\left(\left(n^*+\frac{1}{2}\right)N\varphi\right)+\mathrm{i}\sum_{n^*=0}^{\infty}\underbrace{c_{n^*}^{\mathcal{S}}H_{n^*N}^{'(2)}(kr_0)}_{V_{n^*}^{\mathcal{S},inc}(kr_0)}\cos\left(n^*N\varphi\right). \tag{22}$$

3.4. Spatially distributed source in the exterior zone

Line sources cause problems in finite element codes, e.g., computational aeroacoustics, due to the logarithmic singularity at the source position. Thus, in the past, spatially distributed sources have been developed (Morris, 1995; Sherer, 2004). In general, these sources are derived by the use of the Hankel transform (Morris, 1995). An analytical expression for the sound field generated by a disk source positioned at the origin of the polar coordinate system was found:

$$p_{inc}(r,\varphi)=\begin{cases}\frac{R^*}{k}\left(1-\frac{\mathrm{i}\pi}{2}\right)H_1^{(2)}(kR^*)J_0(kr) & r<R^*\\ -\frac{R^*}{k}\frac{\mathrm{i}\pi}{2}H_0^{(2)}(kr)J_1(kR^*) & r>R^*\end{cases}, \tag{23}$$

where R^* is the radius of the disk source. Applying Graf's addition theorem for Bessel functions, the disk source can be arbitrarily positioned in zone (II). Then, the incident sound pressure is calculated by:

$$\begin{aligned}p_{inc}^{(I)}(r,\varphi)=&\sum_{n^*=0}^{\infty}\underbrace{\delta_{n^*}\frac{-\mathrm{i}\pi\mathrm{R}^*}{2k}H_{n^*}^{(2)}\left(kr^*\right)J_{n^*}(kr)J_1\left(kR^*\right)}_{P_{n^*}^{inc}(kr)}\cos\left(n^*\left(\varphi-\varphi^*\right)\right)\\ =&\sum_{n^*=0}^{\infty}P_{n^*}^{inc}(kr)\sin\left(n^*\varphi^*\right)\sin\left(n^*\varphi\right)+\sum_{n^*=0}^{\infty}P_{n^*}^{inc}(kr)\cos\left(n^*\varphi^*\right)\cos\left(n^*\varphi\right),\end{aligned} \tag{24}$$

and the incident particle velocity by:

$$\begin{aligned}Z_0v_{r,inc}^{(I)}(r,\varphi)=&\mathrm{i}\sum_{n^*=0}^{\infty}\underbrace{\delta_{n^*}\frac{-\mathrm{i}\pi\mathrm{R}^*}{2k}H_{n^*}^{(2)}\left(kr^*\right)J_{n^*}^{'}(kr)J_1\left(kR^*\right)}_{V_{n^*}^{inc}(kr)}\cos\left(n^*\left(\varphi-\varphi^*\right)\right)\\ =&\mathrm{i}\sum_{n^*=0}^{\infty}V_{n^*}^{inc}(kr)\sin\left(n^*\varphi^*\right)\sin\left(n^*\varphi\right)+\mathrm{i}\sum_{n^*=0}^{\infty}V_{n^*}^{inc}(kr)\cos\left(n^*\varphi^*\right)\cos\left(n^*\varphi\right).\end{aligned} \tag{25}$$

3.5. Plane wave

Similar to the line source in the exterior domain, the sound field of an incident plane wave can also be calculated by an infinite mode sum (Flax et al., 1980). The incident sound pressure is calculated by:

$$\begin{aligned} p_{inc}^{(I)}(r,\varphi) =& \sum_{n^*=0}^{\infty} \underbrace{\delta_{n^*} \mathrm{i}^{n^*} J_{n^*}(kr)}_{P_{n^*}^{inc}(kr)} \cos\left(n^*\left(\varphi-\varphi^*\right)\right) \\ =& \sum_{n^*=0}^{\infty} P_{n^*}^{inc}(kr) \sin\left(n^*\varphi^*\right) \sin\left(n^*\varphi\right) + \sum_{n^*=0}^{\infty} P_{n^*}^{inc}(kr) \cos\left(n^*\varphi^*\right) \cos\left(n^*\varphi\right), \end{aligned} \tag{26}$$

and the incident particle velocity by:

$$\begin{aligned} Z_0 v_{r,inc}^{(I)}(r,\varphi) =& \mathrm{i} \sum_{n^*=0}^{\infty} \underbrace{\delta_{n^*} \mathrm{i}^{n^*} J'_{n^*}(kr)}_{V_{n^*}^{inc}(kr)} \cos\left(n^*\left(\varphi-\varphi^*\right)\right) \\ =& \mathrm{i} \sum_{n^*=0}^{\infty} V_{n^*}^{inc}(kr) \sin\left(n^*\varphi^*\right) \sin\left(n^*\varphi\right) + \mathrm{i} \sum_{n^*=0}^{\infty} V_{n^*}^{inc}(kr) \cos\left(n^*\varphi^*\right) \cos\left(n^*\varphi\right), \end{aligned} \tag{27}$$

where φ^* is the incident angle of the plane wave.

4. Matching conditions

Two boundary conditions of field matching were required for the determination of the unknown mode amplitudes a, b:

$$p^{(II)}(r_0,\varphi) \stackrel{!}{=} p_{scat}^{(I)}(r_0,\varphi) + p_{inc}^{(I)}(r_0,\varphi) \qquad \texttt{in} \quad \varphi = (-\varphi_0, \varphi_0) \tag{28}$$

$$Z_0 v_{r,scat}^{(I)}(r_0,\varphi) \stackrel{!}{=} \begin{cases} Z_0 v_r^{(II)}(r_0,\varphi) - Z_0 v_{r,inc}^{(I,II)}(r_0,\varphi) & \texttt{in} \quad \varphi = (-\varphi_0, \varphi_0), \\ Z_0 v_{vib}(r_0,\varphi) - Z_0 v_{r,inc}^{(I)}(r_0,\varphi) & \text{rest of the cylinder.} \end{cases} \tag{29}$$

In Eq. 28 the mode orthogonality in (II) and in Eq. 29 the mode orthogonality in (I) were used. To this end, both sides of Eq. 28 and 29 are multiplied with a mode of the relevant zone with arbitrary but fixed mode orders n, $(\eta + 1/2)\,N$ or ηN, respectively, and are integrated over the range of orthogonality as in Mechel (2005), resulting in four linear systems of equations for $a_n^{\mathcal{A}}$, $a_n^{\mathcal{S}}$, $b_{(\eta+1/2)N}^{\mathcal{S}}$, $b_{\eta N}^{\mathcal{S}}$. In section 5, they will be used to derive the analytic solution of the PAC-MAN model.

4.1. Sound pressure

First, on both sides of the matching condition of the sound pressures (Eq. 28) the integrals

$$\frac{1}{2\varphi_0} \int_{-\varphi_0}^{\varphi_0} \ldots \sin(\iota_1 \varphi)\, \mathrm{d}\varphi \qquad \text{and} \qquad \frac{1}{2\varphi_0} \int_{-\varphi_0}^{\varphi_0} \ldots \cos(\iota_2 \varphi)\, \mathrm{d}\varphi$$

were applied for the anti-symmetric and symmetric part, respectively, with ι from the range of values of $\nu_{\mathcal{A}}$ and $\nu_{\mathcal{S}}$. This resulted on the left-hand side in

$$\sum_{\eta=0}^{\infty} \left\{ b_{(\eta+\frac{1}{2})N}^{\mathcal{A}} \frac{\delta_{(\eta+\frac{1}{2})N,\iota_1}}{2} J_{(\eta+\frac{1}{2})N}(kr_0) \right\} = b_{\iota_1}^{\mathcal{A}} \frac{J_{\iota_1}(kr_0)}{2} \tag{30}$$

and

$$\sum_{\eta=0}^{\infty}\left\{b_{\eta N}^{\mathcal{S}}\frac{\delta_{\eta N,\iota_2}}{\delta_{\iota_2}}J_{\eta N}\left(kr_0\right)\right\}=b_{\iota_2}^{\mathcal{S}}\frac{J_{\iota_2}\left(kr_0\right)}{\delta_{\iota_2}} \tag{31}$$

for the anti-symmetric and the symmetric part, respectively. On the right-hand side, this resulted in

$$\sum_{n=0}^{\infty}a_n^{\mathcal{A}}H_n^{(2)}\left(kr_0\right)I_{n,\iota_1}^{\sin}+\sum_{n^*=0}^{\infty}P_{n^*}^{inc}\left(kr_0\right)\sin\left(n^*\varphi^*\right)I_{n^*,\iota_1}^{\sin} \tag{32}$$

and

$$\sum_{n=0}^{\infty}a_n^{\mathcal{S}}H_n^{(2)}\left(kr_0\right)I_{n,\iota_2}^{\cos}+\sum_{n^*=0}^{\infty}P_{n^*}^{inc}\left(kr_0\right)\cos\left(n^*\varphi^*\right)I_{n^*,\iota_2}^{\cos} \tag{33}$$

for the anti-symmetric and the symmetric part, respectively. In Eqs. 30 to 33, the following integrals were introduced:

$$I_{x,y}^{\sin}=\frac{1}{2\varphi_0}\int_{-\varphi_0}^{\varphi_0}\sin\left(x\varphi\right)\sin\left(y\varphi\right)\mathrm{d}\varphi, \tag{34}$$

$$I_{x,y}^{\cos}=\frac{1}{2\varphi_0}\int_{-\varphi_0}^{\varphi_0}\cos\left(x\varphi\right)\cos\left(y\varphi\right)\mathrm{d}\varphi. \tag{35}$$

In total, the matching condition for the sound pressure resulted in:

$$b_{\iota_1}^{\mathcal{A}}\frac{J_{\iota_1}\left(kr_0\right)}{2}=\sum_{n=0}^{\infty}a_n^{\mathcal{A}}H_n^{(2)}\left(kr_0\right)I_{n,\iota_1}^{\sin}+\sum_{n^*=0}^{\infty}P_{n^*}^{inc}\left(kr_0\right)\sin\left(n^*\varphi^*\right)I_{n^*,\iota_1}^{\sin} \tag{36}$$

for the anti-symmetric part and

$$b_{\iota_2}^{\mathcal{S}}\frac{J_{\iota_2}\left(kr_0\right)}{\delta_{\iota_2}}=\sum_{n=0}^{\infty}a_n^{\mathcal{S}}H_n^{(2)}\left(kr_0\right)I_{n,\iota_2}^{\cos}+\sum_{n^*=0}^{\infty}P_{n^*}^{inc}\left(kr_0\right)\cos\left(n^*\varphi^*\right)I_{n^*,\iota_2}^{\cos} \tag{37}$$

for the symmetric part. These are two linear homogeneous systems of equations for the vectors of unknown mode amplitudes $\left\{b_{\iota_1}^{\mathcal{A}},a_n^{\mathcal{A}}\right\}$ and $\left\{b_{\iota_2}^{\mathcal{S}},a_n^{\mathcal{S}}\right\}$.

4.2. Particle velocity

Second, on both sides of the matching condition for the particle velocity (Eq. 28) the integrals

$$\frac{1}{2\pi}\int_0^{2\pi}\ldots\sin\left(i_1\varphi\right)\mathrm{d}\varphi\qquad\text{and}\qquad\frac{1}{2\pi}\int_0^{2\pi}\ldots\cos\left(i_2\varphi\right)\mathrm{d}\varphi$$

were applied for the anti-symmetric and the symmetric part, respectively, with i_1 and i_2 from the range of values of n. The left-hand side from Eq. 28 resulted in

$$\mathrm{i}\sum_{n=0}^{\infty}a_n^{\mathcal{A}}\frac{\delta_{n,i_1}-\delta_{n,0}\delta_{i_1,0}}{2}H_n^{\prime(2)}\left(kr_0\right)=\mathrm{i}\frac{1-\delta_{i_1,0}}{2}H_{i_1}^{\prime(2)}\left(kr_0\right)a_{i_1}^{\mathcal{A}} \tag{38}$$

for the anti-symmetric part and

$$\mathrm{i}\sum_{n=0}^{\infty}a_n^{\mathcal{S}}\frac{\delta_{n,i_2}}{\delta_n}H_n^{\prime(2)}\left(kr_0\right)=\mathrm{i}\frac{1}{\delta_{i_2}}H_{i_2}^{\prime(2)}\left(kr_0\right)a_{i_2}^{\mathcal{S}} \tag{39}$$

for the symmetric part.

The first line of the right-hand side of Eq. 28 took the form

$$\frac{1}{2\pi}\int_{-\varphi_0}^{\varphi_0} Z_0 v_r^{(II)}\left(r_0,\varphi\right)\left\{\sin\left(i_1\varphi\right)+\cos\left(i_2\varphi\right)\right\}\mathrm{d}\varphi-\frac{1}{2\pi}\int_{-\varphi_0}^{\varphi_0} Z_0 v_{r,inc}^{(I)}\left(r_0,\varphi\right)\left\{\sin\left(i_1\varphi\right)+\cos\left(i_2\varphi\right)\right\}\mathrm{d}\varphi \tag{40}$$

and contributed:

$$\mathrm{i}\sum_{\eta=0}^{\infty} b_{\left(\eta+\frac{1}{2}\right)N}^{\mathcal{A}} J'_{\left(\eta+\frac{1}{2}\right)N}\left(kr_0\right) I_{i_1,\left(\eta+\frac{1}{2}\right)N}^{'\sin}-\mathrm{i}\sum_{n^*=0}^{\infty} V_{n^*}^{inc}\left(kr_0\right)\sin\left(n^*\varphi^*\right) I_{i_1,n^*}^{'\sin} \tag{41}$$

to the anti-symmetric part and

$$\mathrm{i}\sum_{\eta=0}^{\infty} b_{\eta N}^{\mathcal{S}} J'_{\eta N}\left(kr_0\right) I_{i_2,\eta N}^{'\cos}-\mathrm{i}\sum_{n^*=0}^{\infty} V_{n^*}^{inc}\left(kr_0\right)\cos\left(n^*\varphi^*\right) I_{i_2,n^*}^{'\cos} \tag{42}$$

to the symmetric part. In these equations, the following integrals were introduced:

$$I_{x,y}^{'\sin}=\frac{1}{2\pi}\int_{-\varphi_0}^{\varphi_0}\sin\left(x\varphi\right)\sin\left(y\varphi\right)\mathrm{d}\varphi=\frac{\varphi_0}{\pi} I_{x,y}^{\sin}, \tag{43}$$

$$I_{x,y}^{'\cos}=\frac{1}{2\pi}\int_{-\varphi_0}^{\varphi_0}\cos\left(x\varphi\right)\cos\left(y\varphi\right)\mathrm{d}\varphi=\frac{\varphi_0}{\pi} I_{x,y}^{\cos}. \tag{44}$$

The second line of the right-hand side of Eq. 28 gave:

$$\begin{aligned}&\frac{1}{2\pi}\int_{0}^{2\pi} Z_0 v_{vib}\left(r_0,\varphi\right)\left\{\sin\left(i_1\varphi\right)+\cos\left(i_2\varphi\right)\right\}\mathrm{d}\varphi-\frac{1}{2\pi}\int_{-\varphi_0}^{\varphi_0} Z_0 v_{vib}\left(r_0,\varphi\right)\left\{\sin\left(i_1\varphi\right)+\cos\left(i_2\varphi\right)\right\}\mathrm{d}\varphi\\ &-\frac{1}{2\pi}\int_{0}^{2\pi} Z_0 v_{r,inc}^{(I)}\left(r_0,\varphi\right)\left\{\sin\left(i_1\varphi\right)+\cos\left(i_2\varphi\right)\right\}\mathrm{d}\varphi+\frac{1}{2\pi}\int_{-\varphi_0}^{\varphi_0} Z_0 v_{r,inc}^{(I)}\left(r_0,\varphi\right)\left\{\sin\left(i_1\varphi\right)+\cos\left(i_2\varphi\right)\right\}\mathrm{d}\varphi,\end{aligned} \tag{45}$$

whereof the first line contributed

$$\underbrace{\sum_{n^*=0}^{\infty} Z_0 V_{n^*}^{\mathcal{A},vib}\frac{\delta_{i_1,n^*}-\delta_{i_1,0}\delta_{n^*,0}}{2}}_{Z_0 V_{i_1}^{\mathcal{A},vib}\frac{1-\delta_{i_1,0}}{2}}-\sum_{n^*=0}^{\infty} Z_0 V_{n^*}^{\mathcal{A},vib} I_{i_1,n^*}^{'\sin} \tag{46}$$

to the anti-symmetric and

$$\underbrace{\sum_{n^*=0}^{\infty} Z_0 V_{n^*}^{\mathcal{S},vib}\frac{\delta_{n^*,i_2}}{\delta_{n^*}}}_{Z_0 V_{i_2}^{\mathcal{S},vib}\frac{1}{\delta_{i_2}}}-\sum_{n^*=0}^{\infty} Z_0 V_{n^*}^{\mathcal{S},vib} I_{i_2,n^*}^{'\cos} \tag{47}$$

to the symmetric part. The second line contributed

$$\underbrace{-\mathrm{i}\sum_{n^*=0}^{\infty} V_{n^*}^{inc}\left(kr_0\right)\sin\left(n^*\varphi^*\right)\frac{\delta_{i_1,n^*}-\delta_{i_1,0}\delta_{n^*,0}}{2}}_{V_{i_1}^{inc}(kr_0)\sin(i_1\varphi^*)\frac{1}{2}}+\mathrm{i}\sum_{n^*=0}^{\infty} V_{n^*}^{inc}\left(kr_0\right)\sin\left(n^*\varphi^*\right) I_{i_1,n^*}^{'\sin} \tag{48}$$

to the anti-symmetric part and

$$-\mathrm{i}\underbrace{\sum_{n^*=0}^{\infty} V_{n^*}^{inc}\left(kr_0\right)\cos\left(n^*\varphi^*\right)\frac{\delta_{i_2,n^*}}{\delta_{i_2}}}_{V_{i_2}^{inc}(kr_0)\cos(i_2\varphi^*)\frac{1}{\delta_{i_2}}}+\mathrm{i}\sum_{n^*=0}^{\infty} V_{n^*}^{inc}\left(kr_0\right)\cos\left(n^*\varphi^*\right)I_{i_2,n^*}^{'\cos} \tag{49}$$

to the symmetric part.

In total and already simplified, the matching condition for v_r resulted in

$$\begin{aligned}\mathrm{i}\frac{1-\delta_{i_1,0}}{2}H_{i_1}^{'(2)}\left(kr_0\right)a_{i_1}^{\mathcal{A}} = \mathrm{i}\sum_{\eta=0}^{\infty}\left\{b_{(\eta+\frac{1}{2})N}^{\mathcal{A}}J'_{(\eta+\frac{1}{2})N}\left(kr_0\right)I_{i_1,(\eta+\frac{1}{2})N}^{'\sin}\right\}\\ +\frac{1-\delta_{i_1,0}}{2}Z_0V_{i_1}^{\mathcal{A},vib}-\sum_{n^*=0}^{\infty}Z_0V_{n^*}^{\mathcal{A},vib}I_{i_1,n^*}^{'\sin}\\ -\mathrm{i}\frac{1}{2}V_{i_1}^{inc}\left(kr_0\right)\sin\left(i_1\varphi^*\right)\end{aligned} \tag{50}$$

for the anti-symmetric part and

$$\begin{aligned}\mathrm{i}\frac{1}{\delta_{i_2}}H_{i_2}^{'(2)}\left(kr_0\right)a_{i_2}^{\mathcal{S}} = \mathrm{i}\sum_{\eta=0}^{\infty}\left\{b_{\eta N}^{\mathcal{S}}J'_{\eta N}\left(kr_0\right)I_{i_2,\eta N}^{'\cos}\right\}\\ +\frac{1}{\delta_{i_2}}Z_0V_{i_2}^{\mathcal{S},vib}-\sum_{n^*=0}^{\infty}Z_0V_{n^*}^{\mathcal{S},vib}I_{i_2,n^*}^{'\cos}\\ -\mathrm{i}\frac{1}{\delta_{i_2}}V_{i_2}^{inc}\left(kr_0\right)\cos\left(i_2\varphi^*\right)\end{aligned} \tag{51}$$

for the symmetric part. These are the third and fourth linear in-homogeneous systems of equations for the vectors of unknowns $\left\{a_{i_1}^{\mathcal{A}}, b_{(\eta+\frac{1}{2})N}^{\mathcal{A}}\right\}$ and $\left\{a_{i_2}^{\mathcal{S}}, b_{\eta N}^{\mathcal{S}}\right\}$.

5. The PAC-MAN equations

Finally, the retrieved equation systems (Eqs. 36, 37, 50 and 51) were combined to derive the analytic solution of the PAC-MAN model which we call the PAC-MAN equations. To this end, the b_ι were eliminated from Eq. 36 and 37 and inserted into Eq. 50 and 51:

$$b_{(\eta+\frac{1}{2})N}^{\mathcal{A}} = \frac{2}{J_{(\eta+\frac{1}{2})N}\left(kr_0\right)}\left\{\sum_{n=0}^{\infty}a_n^{\mathcal{A}}H_n^{(2)}\left(kr_0\right)I_{n,(\eta+\frac{1}{2})N}^{\sin}+\sum_{n^*=0}^{\infty}P_{n^*}^{inc}\left(kr_0\right)\sin\left(n^*\varphi^*\right)I_{n^*,(\eta+\frac{1}{2})N}^{\sin}\right\} \tag{52}$$

and

$$b_{\eta N}^{\mathcal{S}} = \frac{\delta_{\eta N}}{J_{\eta N}\left(kr_0\right)}\left\{\sum_{n=0}^{\infty}a_n^{\mathcal{S}}H_n^{(2)}\left(kr_0\right)I_{n,\eta N}^{\cos}+\sum_{n^*=0}^{\infty}P_{n^*}^{inc}\left(kr_0\right)\cos\left(n^*\varphi^*\right)I_{n^*,\eta N}^{\cos}\right\}. \tag{53}$$

After insertion in Eq. 50 and 51 and after rearrangement those equations became:

$$\begin{aligned}
&\sum_{n=0}^{\infty}\left\{\frac{\delta_{n,i}-\delta_{n,0}}{2}H_i^{'(2)}\left(kr_0\right)-\frac{\varphi_0}{\pi}H_n^{(2)}\left(kr_0\right)\sum_{\eta=0}^{\infty}\frac{2J'_{(\eta+\frac{1}{2})N}\left(kr_0\right)}{J_{(\eta+\frac{1}{2})N}\left(kr_0\right)}I^{\sin}_{n,(\eta+\frac{1}{2})N}I^{\sin}_{i,(\eta+\frac{1}{2})N}\right\}a_n^{\mathcal{A}}\\
=&\frac{\varphi_0}{\pi}\sum_{\eta=0}^{\infty}\left\{\frac{2J'_{(\eta+\frac{1}{2})N}\left(kr_0\right)}{J_{(\eta+\frac{1}{2})N}\left(kr_0\right)}I^{\sin}_{i,(\eta+\frac{1}{2})N}\sum_{n^*=0}^{\infty}\left[P^{inc}_{n^*}\left(kr_0\right)\sin\left(n^*\varphi^*\right)I^{\sin}_{n^*,(\eta+\frac{1}{2})N}\right]\right\}\\
&-\mathrm{i}\frac{1-\delta_{i,0}}{2}Z_0V_i^{\mathcal{A},vib}+\mathrm{i}\frac{\varphi_0}{\pi}\sum_{n^*=0}^{\infty}Z_0V_{n^*}^{\mathcal{A},vib}I^{\sin}_{i,n^*}-\frac{1}{2}V_i^{inc}\left(kr_0\right)\sin\left(i\varphi^*\right)
\end{aligned}\tag{54}$$

for the anti-symmetric part and

$$\begin{aligned}
&\sum_{n=0}^{\infty}\left\{\frac{\delta_{n,i}}{\delta_i}H_i^{'(2)}\left(kr_0\right)-\frac{\varphi_0}{\pi}H_n^{(2)}\left(kr_0\right)\sum_{\eta=0}^{\infty}\frac{\delta_{\eta N}J'_{\eta N}\left(kr_0\right)}{J_{\eta N}\left(kr_0\right)}I^{\cos}_{n,\eta N}I^{\cos}_{i,\eta N}\right\}a_n^{\mathcal{S}}\\
=&\frac{\varphi_0}{\pi}\sum_{\eta=0}^{\infty}\left\{\frac{\delta_{\eta N}J'_{\eta N}\left(kr_0\right)}{J_{\eta N}\left(kr_0\right)}I^{\cos}_{i,\eta N}\sum_{n^*=0}^{\infty}\left[P^{inc}_{n^*}\left(kr_0\right)\cos\left(n^*\varphi^*\right)I^{\cos}_{n^*,\eta N}\right]\right\}\\
&-\mathrm{i}\frac{1}{\delta_i}Z_0V_i^{\mathcal{S},vib}+\mathrm{i}\frac{\varphi_0}{\pi}\sum_{n^*=0}^{\infty}Z_0V_{n^*}^{\mathcal{S},vib}I^{\cos}_{i,n^*}-\frac{1}{\delta_i}V_i^{inc}\left(kr_0\right)\cos\left(i\varphi^*\right)
\end{aligned}\tag{55}$$

for the symmetric part.

These are two equation systems for the unknowns $a_n^{\mathcal{A}}$ and $a_n^{\mathcal{S}}$ which in principle have an infinite size. The precision and the computational cost of the sound field calculation depend on the truncation order of the infinite sums. To investigate the effect of the truncation order, the relative change of the sound field as a function of the truncation order was evaluated. The relative change e_2 of the solution is defined as

$$e_2\left(M\right)=\frac{\left\|p_M\left(r\right)-p_{M-1}\left(r\right)\right\|_2}{\left\|p_{M-1}\left(r\right)\right\|_2},\tag{56}$$

where M is the truncation order and $p_M\left(r\right)$ is the sound pressure calculated at distance r with a truncation order of M. For the evaluation, a line source was placed at $r^*=4\,\mathrm{m}$ and $\varphi^*=\pi/4$. The surface vibration was set to zero. The sound field was evaluated at $r=2\,\mathrm{m}$ for PAC-MAN models with $r_0=1\,\mathrm{m}$ and various angular widths of the cut out. Figure 2 shows e_2 for different frequencies and $N=6$. Figure 3 shows e_2 for a frequency of 1000 Hz and $N=4,6,8,10$. For 250 and 1000 Hz, e_2 decreased below 0.1% for a truncation order greater than 40. For 4000 Hz, the truncation order had to be greater than 100 to achieve a similar numerical accuracy as for 250 and 1000 Hz in the calculations.

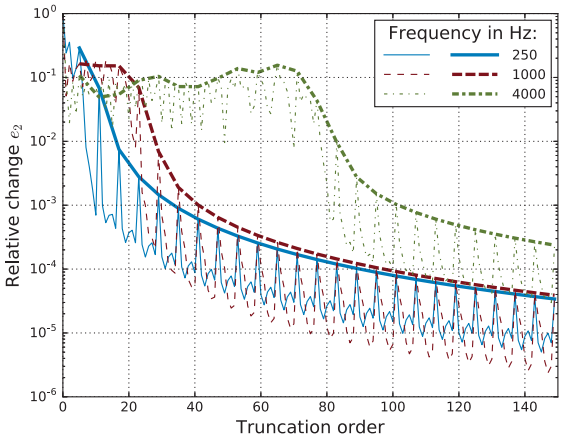

Figure 2: Relative change for all considered truncation orders < 150 (thin lines) and moving maximum of the relative change (thick lines) illustrating the numerical accuracy of the PAC-MAN model as a function of the truncation order for various frequencies ($f = 250$ Hz with $kr_0 = 4.58$, $f = 1000$ Hz with $kr_0 = 18.32$, and $f = 4000$ Hz with $kr_0 = 73.27$) and a PAC-MAN constant $N = 6$.

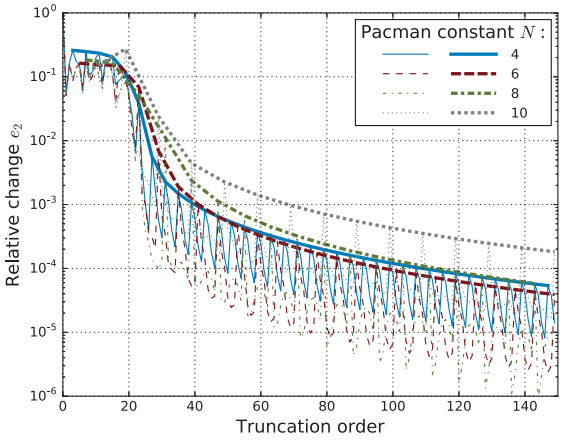

Figure 3: Relative change for all considered truncation orders < 150 (thin lines) and moving maximum of the relative change (thick lines) illustrating the numerical accuracy of the PAC-MAN model as a function of the truncation order for various PAC-MAN constants ($N = 4, 6, 8, 10$) and a frequency of 1000 Hz ($kr_0 = 18.32$).

6. Numerical Examples

In the following, results for various radiation and scattering examples are presented. In all examples, the sound pressure field was evaluated at octave band center frequencies between 16 and 4000 Hz and the truncation order was set to 100. In the radiation example, $V_{n^*}^{inc}$ and $P_{n^*}^{inc}$ were set to zero. In the scattering examples, there was no initial vibration on the surface of the PAC-MAN model, thus, $Z_0 v_{vib} = 0$. In all calculations, mode coupling integrals were calculated analytically (see Appendix B). Results are plotted as radiation and scattering patterns, which show the normalized sound pressure amplitude $|p(r,\varphi)|/\max_\varphi |p(r,\varphi)|$ of the radiated or scattered field as a function of φ for $r = 2$m.

6.1. Symmetric radiation

In the first example, the symmetric radiation of a surface vibration was considered. Since there was no incident field, $V_{n^*}^{inc} = P_{n^*}^{inc} = 0$. All mode amplitudes of the surface vibration were set to zero except $V_0^{\mathcal{S},vib}$ which was set to $0.1 m/s$ and, thus, Eq. 55 had to be evaluated only. Results are shown in Figure 4.

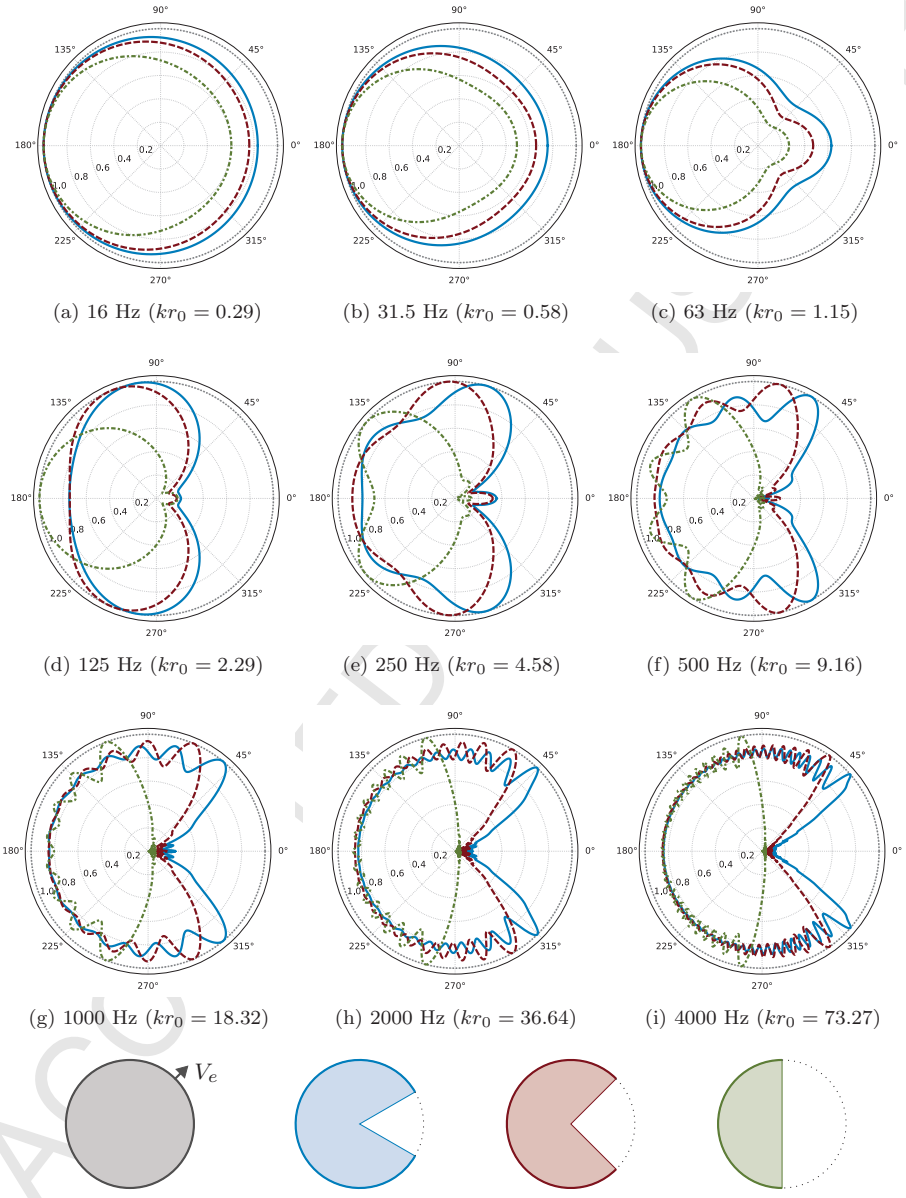

(a) 16 Hz ($kr_0 = 0.29$) (b) 31.5 Hz ($kr_0 = 0.58$) (c) 63 Hz ($kr_0 = 1.15$)

(d) 125 Hz ($kr_0 = 2.29$) (e) 250 Hz ($kr_0 = 4.58$) (f) 500 Hz ($kr_0 = 9.16$)

(g) 1000 Hz ($kr_0 = 18.32$) (h) 2000 Hz ($kr_0 = 36.64$) (i) 4000 Hz ($kr_0 = 73.27$)

(j) Sketch of a full cylinder and of PAC-MAN models with $N = 6, 4, 2$ (from left to right). Colors correspond to the lines in **a-i**.

Figure 4: Radiation patterns for various frequencies (**a-i**) of the PAC-MAN model with $N = 6$ (———), $N = 4$ (- - - - - -) and $N = 2$ (-·-·-·-·-) and of a full cylinder (·····) for comparison. Infinite sums were truncated at order 100. r_0 was 1 m and the radiation patterns were evaluated at 1024 points located on an equiangular circular grid with $r = 2$ m.

6.2. Line source in the exterior zone

In this example, we considered the symmetric scattering of a cylindrical wave emitted by a line source positioned at $r^* = 4\,\mathrm{m}$ and $\varphi^* = 0$. Since in the symmetric case all $a_n^{\mathcal{A}}$ are zero, we again had to evaluate Eq. 55 only. Results are shown in Figure 5 for various frequencies.

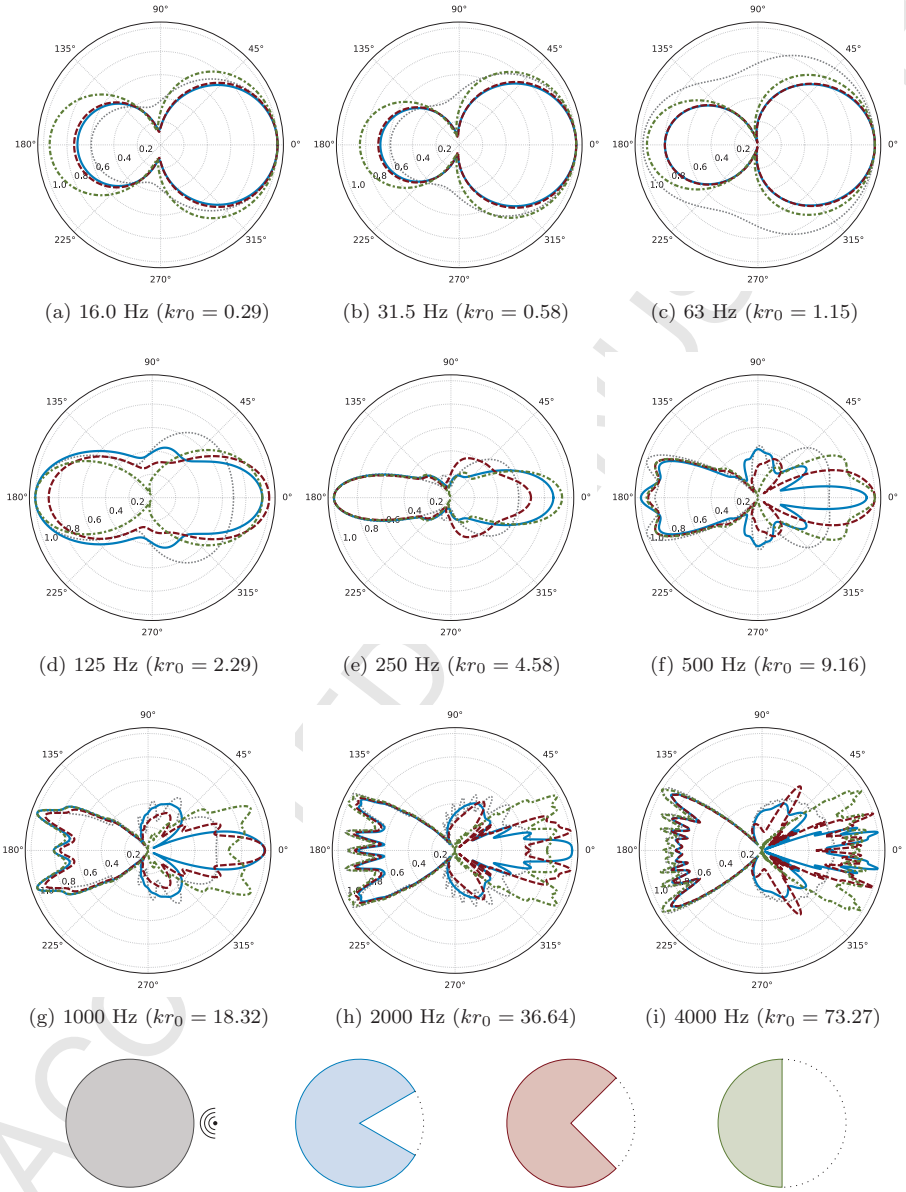

(a) 16.0 Hz ($kr_0 = 0.29$) (b) 31.5 Hz ($kr_0 = 0.58$) (c) 63 Hz ($kr_0 = 1.15$)

(d) 125 Hz ($kr_0 = 2.29$) (e) 250 Hz ($kr_0 = 4.58$) (f) 500 Hz ($kr_0 = 9.16$)

(g) 1000 Hz ($kr_0 = 18.32$) (h) 2000 Hz ($kr_0 = 36.64$) (i) 4000 Hz ($kr_0 = 73.27$)

(j) Sketch of a full cylinder (also the incident field is indicated) and of PAC-MAN models with $N = 6, 4, 2$ (from left to right). Colors correspond to the lines in **a-i**.

Figure 5: Scattering patterns for various frequencies (**a-i**) of the PAC-MAN model with $N = 6$ (———), $N = 4$ (- - - - - -) and $N = 2$ (-·-·-·-·-) and of a full cylinder (·····) for comparison. The incident field was a cylindrical wave, symmetric with respect to the x-axis. The origin of the cylindrical wave was located at $r^* = 4\mathrm{m}$ and $\varphi^* = 0$. Other details as in Figure 4.

In the next example, we considered an arbitrarily positioned line source. r^* was 4 m and φ^* was $\pi/4$. Thus, we had to evaluate Eq. 54 and 55 to retrieve $a_n^{\mathcal{A}}$ and $a_n^{\mathcal{S}}$. Results are shown in Figure 6 for the same frequencies as in Figure 5.

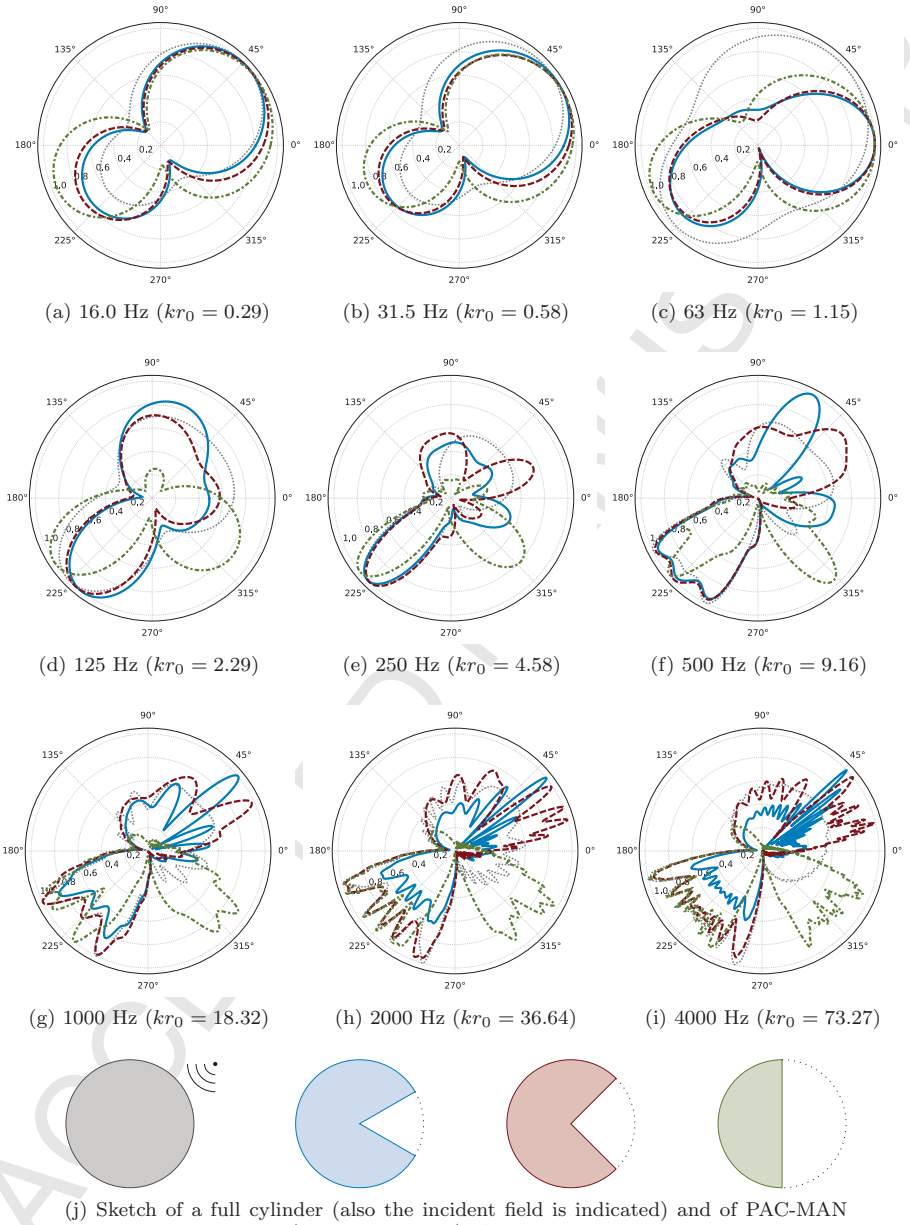

(a) 16.0 Hz ($kr_0 = 0.29$) (b) 31.5 Hz ($kr_0 = 0.58$) (c) 63 Hz ($kr_0 = 1.15$)

(d) 125 Hz ($kr_0 = 2.29$) (e) 250 Hz ($kr_0 = 4.58$) (f) 500 Hz ($kr_0 = 9.16$)

(g) 1000 Hz ($kr_0 = 18.32$) (h) 2000 Hz ($kr_0 = 36.64$) (i) 4000 Hz ($kr_0 = 73.27$)

(j) Sketch of a full cylinder (also the incident field is indicated) and of PAC-MAN models with $N = 6, 4, 2$ (from left to right). Colors correspond to the lines in **a-i**.

Figure 6: Scattering patterns for various frequencies (**a-i**) of the PAC-MAN model with $N = 6$ (———), $N = 4$ (- - - - - -) and $N = 2$ (·-·-·-·-·-) and of a full cylinder (·····) for comparison. The incident field was a cylindrical wave. The origin of the cylindrical wave was located at $r^* = 4$m and $\varphi^* = \pi/4$. Other details as in Figure 4.

The last numerical example for a line source in the exterior zone was almost identical to the previous one, with the small difference that the line source was positioned very close to a corner of the PAC-MAN model with $r^* = 1.01\,\mathrm{m}$ and $\varphi^* = \pi/N$. Results are shown in Figure 7.

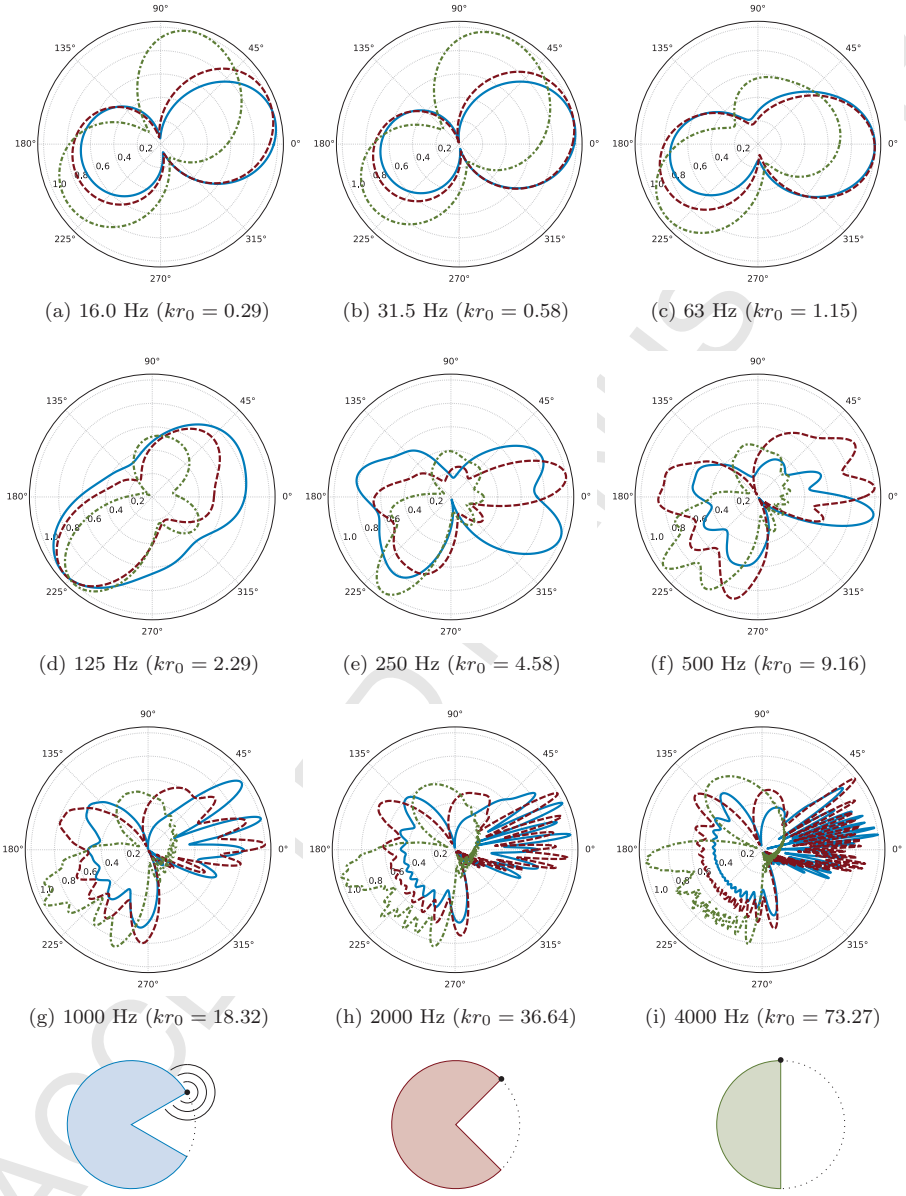

(a) 16.0 Hz ($kr_0 = 0.29$) (b) 31.5 Hz ($kr_0 = 0.58$) (c) 63 Hz ($kr_0 = 1.15$)

(d) 125 Hz ($kr_0 = 2.29$) (e) 250 Hz ($kr_0 = 4.58$) (f) 500 Hz ($kr_0 = 9.16$)

(g) 1000 Hz ($kr_0 = 18.32$) (h) 2000 Hz ($kr_0 = 36.64$) (i) 4000 Hz ($kr_0 = 73.27$)

(j) Sketch of the PAC-MAN models with $N = 6, 4, 2$ (from left to right). The source position and the incident field are indicated. Colors correspond to the lines in **a-i**.

Figure 7: Scattering patterns for various frequencies (**a-i**) of the PAC-MAN model with $N = 6$ (———), $N = 4$ (- - - - - -) and $N = 2$ (·-·-·-·-·-). The origin of the cylindrical wave was located very close to a corner of the PAC-MAN model at $r^* = 1.01\mathrm{m}$ and $\varphi^* = \pi/N$. Other details as in Figure 4.

6.3. Line source in the interior zone

The line source was now positioned in (II). For the calculation of the sound field in (I), first, the mode amplitudes of the sound field in (II) emitted by the line source had to be calculated numerically following Eq. 21 and 22. Second, Eq. 54 and Eq. 55 were solved. Results are shown in Figure 8.

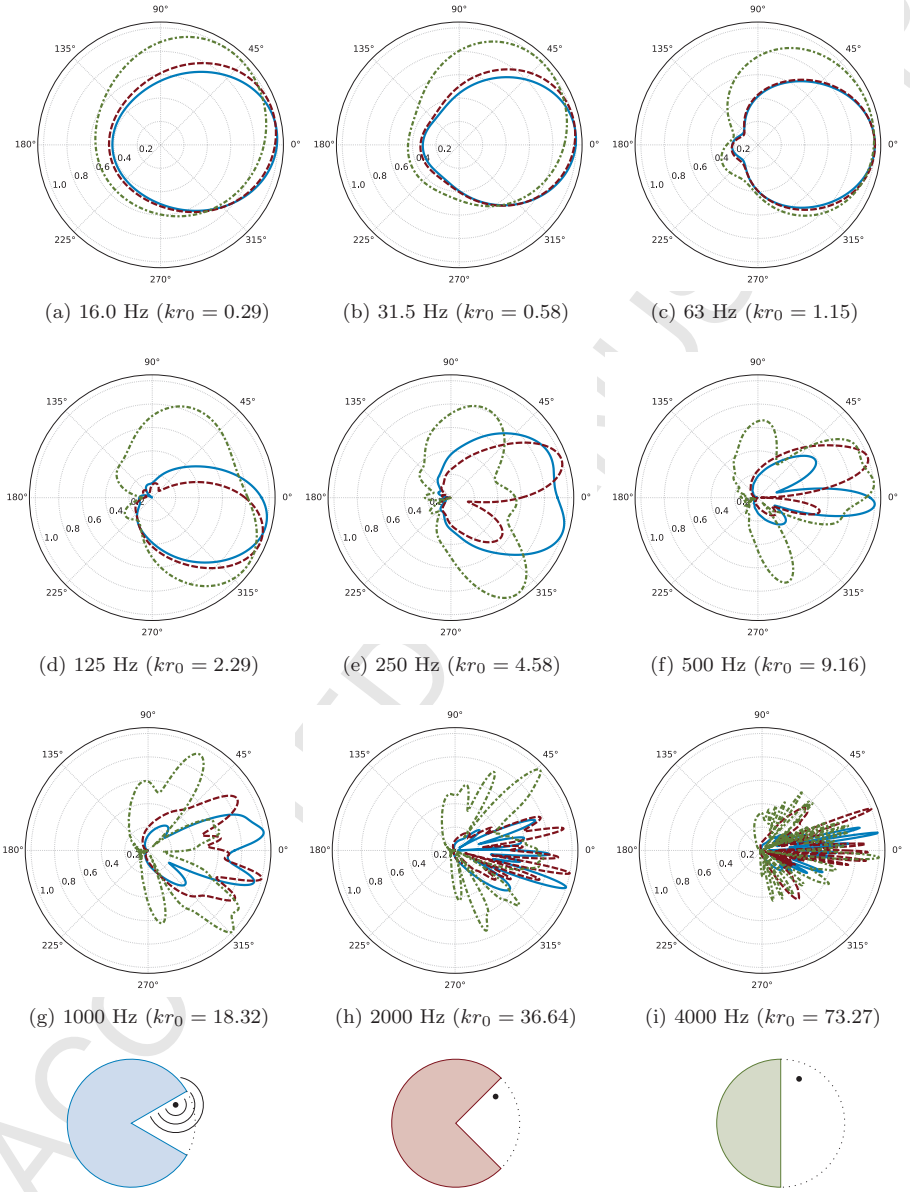

(a) 16.0 Hz ($kr_0 = 0.29$) (b) 31.5 Hz ($kr_0 = 0.58$) (c) 63 Hz ($kr_0 = 1.15$)

(d) 125 Hz ($kr_0 = 2.29$) (e) 250 Hz ($kr_0 = 4.58$) (f) 500 Hz ($kr_0 = 9.16$)

(g) 1000 Hz ($kr_0 = 18.32$) (h) 2000 Hz ($kr_0 = 36.64$) (i) 4000 Hz ($kr_0 = 73.27$)

(j) Sketch of the PAC-MAN models with $N = 6, 4, 2$ (from left to right). The source position and the incident field are indicated. Colors correspond to the lines in **a-i**.

Figure 8: Radiation patterns for various frequencies (**a-i**) of the PAC-MAN model with $N = 6$ (———), $N = 4$ (- - - - - - -) and $N = 2$ (-·-·-·-·-·-) of a line source located in (II). The origin of the cylindrical wave was located at $r_s = 0.75$m and $\varphi_s = {}^{3\pi}/_{4N}$. Other details as in Figure 4.

6.4. Disk source in the exterior zone

This example is almost identical to the example shown in Figure 6 with the difference that a disk source was used instead of a line source. The radius of the disk source R^* was 0.01m. Resulting scattering patterns are shown in Figure 9.

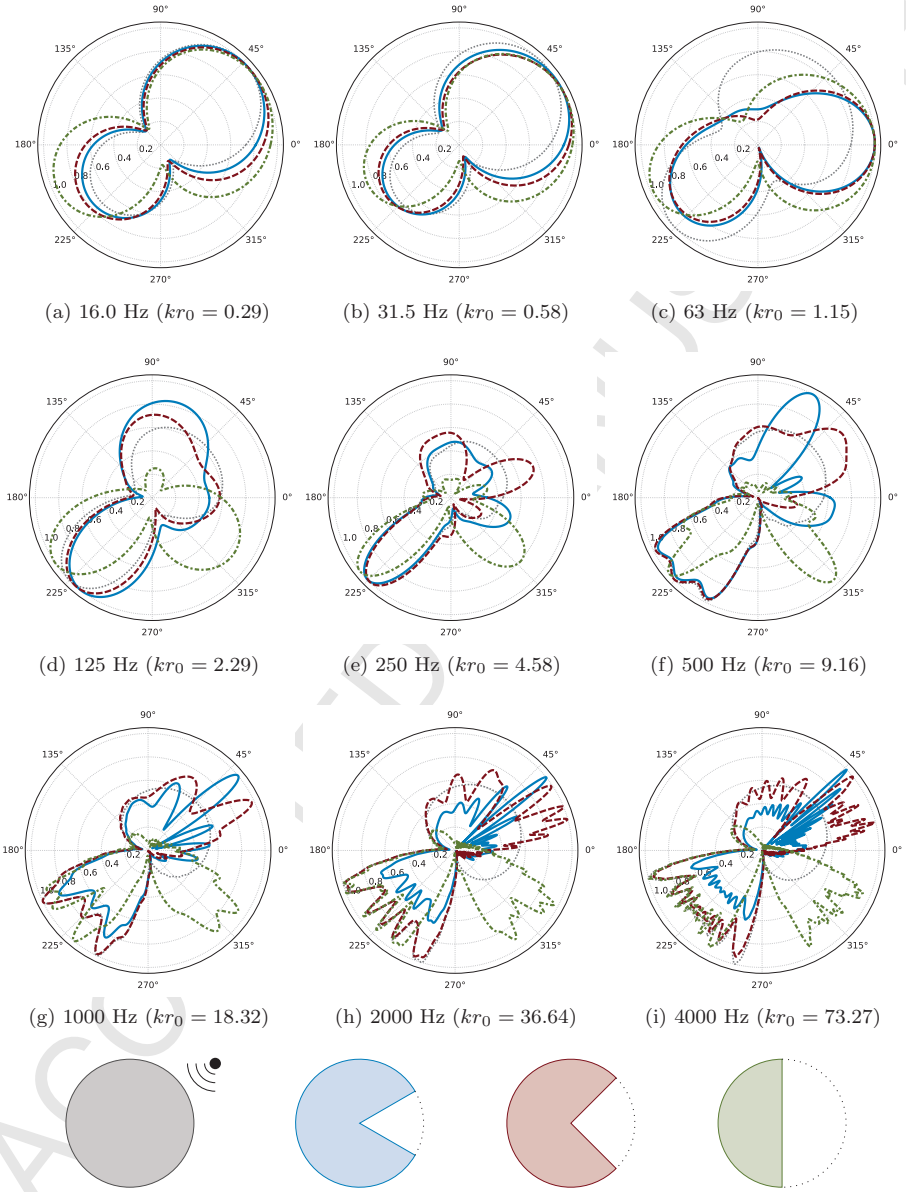

(a) 16.0 Hz ($kr_0 = 0.29$) (b) 31.5 Hz ($kr_0 = 0.58$) (c) 63 Hz ($kr_0 = 1.15$)

(d) 125 Hz ($kr_0 = 2.29$) (e) 250 Hz ($kr_0 = 4.58$) (f) 500 Hz ($kr_0 = 9.16$)

(g) 1000 Hz ($kr_0 = 18.32$) (h) 2000 Hz ($kr_0 = 36.64$) (i) 4000 Hz ($kr_0 = 73.27$)

(j) Sketch of a full cylinder (also the incident field is indicated) and of PAC-MAN models with $N = 6, 4, 2$ (from left to right). Colors correspond to the lines in **a-i**.

Figure 9: Scattering patterns for various frequencies (**a-i**) of the PAC-MAN model with $N = 6$ (———), $N = 4$ (- - - - - - -) and $N = 2$ (-·-·-·-·-) and of a full cylinder (·····) for comparison. The incident field was generated by a spatially distributed axisymmetric source which had a radius of $R^* = 0.01$m and was located at $r^* = 4$m and $\varphi^* = \pi/4$. Other details as in Figure 4.

6.5. Scattering of a plane wave

The last example is almost identical to the scattering of a cylindrical wave originating from a line source in the exterior domain. However, we had to use the incident mode amplitudes for plane waves from Eq. 26 in the calculations. Results are shown in Figure 10.

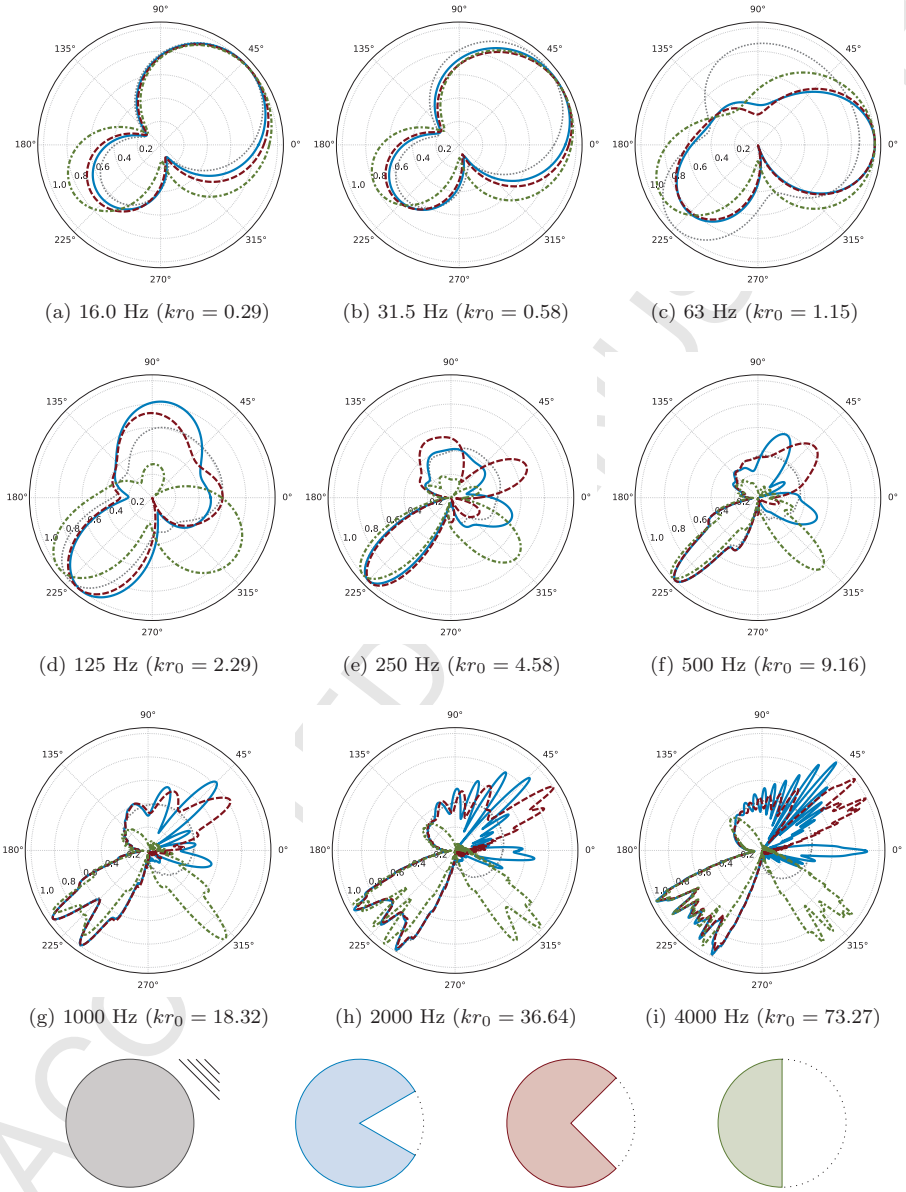

(a) 16.0 Hz ($kr_0 = 0.29$) (b) 31.5 Hz ($kr_0 = 0.58$) (c) 63 Hz ($kr_0 = 1.15$)

(d) 125 Hz ($kr_0 = 2.29$) (e) 250 Hz ($kr_0 = 4.58$) (f) 500 Hz ($kr_0 = 9.16$)

(g) 1000 Hz ($kr_0 = 18.32$) (h) 2000 Hz ($kr_0 = 36.64$) (i) 4000 Hz ($kr_0 = 73.27$)

(j) Sketch of a full cylinder (also the incident field is indicated) and of PAC-MAN models with $N = 6, 4, 2$ (from left to right). Colors correspond to the lines in **a-i**.

Figure 10: Scattering patterns for various frequencies (**a-i**) of the PAC-MAN model with $N = 6$ (———), $N = 4$ (- - - - - -) and $N = 2$ (-·-·-·-) and of a full cylinder (·····) for comparison. The incident field was a plane wave with $\varphi_s = \pi/4$. Other details as in Figure 4.

7. Concluding remarks

In this work we have derived an analytical formulation of the sound field around the PAC-MAN geometry that can be used as a benchmark case in linear acoustic under very general conditions. The analytic solution describes the radiation of surface vibrations, the scattering of plane waves and the scattering of cylindrical waves originating from an arbitrarily positioned line source in the interior or the exterior zone. Since an expansion in terms of cylindrical modes was used in the sound-field formulation, the degrees of freedom associated with this problem were reduced to those of a one-dimensional problem.

The aim of the PAC-MAN model is to provide a benchmark case for two and two and a half dimensional (2.5D) linear acoustic problems. While in Duhamel (1996) and Kasess et al. (2016) the sound field scattered by a simple rigid cylinder was used as benchmark, the PAC-MAN model provides a more complex benchmark case including convex and concave corners in the geometry. In 2.5D calculations, the PAC-MAN model has to be calculated for a set of imaginary and real valued wave numbers to retrieve the 3D sound field. To this end, the Hankel function of the second kind $H^{(2)}(kr)$ and the Bessel function $J(kr)$ just have to be replaced by the modified Hankel function of the second kind $K^{(2)}(kr)$ and the modified Bessel function $I(kr)$, respectively, when imaginary wave numbers need to be simulated.

The sound field formulation of the PAC-MAN model is general enough to be easily extended in various ways. While in the proposed model the angular cut-out width of the PAC-MAN was limited to integer fractions of π, first, an extension of $\nu_{\mathcal{A}}$ and $\nu_{\mathcal{S}}$ from integer to rational numbers would allow an arbitrary angular cut-out width. A second way to extend the PAC-MAN model would be to allow additional zones in the cylinder, e.g., calculating the sound field for an acoustic system consisting of cylindrical layers with various cut-outs in the layers or for a PAC-MAN filled with air at the center of the PAC-MAN. Third, the PAC-MAN equations could be extended to include a normal admittance on the boundary surface in the interior and exterior zone.

Finally, we would like to remark that the scope of this work is much wider than its current application as benchmark case. Since the mode amplitudes of a PAC-MAN could be interpreted as a multipole which describes the geometry and the boundary conditions within a cylindrical domain analytically, the corresponding PAC-MAN equations could be used as a basis for a 2D and 2.5D analytical multipole method. By coupling of various "PAC-MANs", the sound field scattered by arbitrary geometries could be calculated analytically, e.g., sonic crystals consisting of cylinders with a special shape.

Appendix A. Mode orthogonality

In the exterior zone, mode orthogonality follows for $n = 0, 1, 2, \ldots$ and $n' = 0, 1, 2, \ldots$ from the orthogonality of cosine functions

$$\begin{aligned}\frac{1}{2\pi}\int_0^{2\pi} \cos(n\varphi)\cos\left(n'\varphi\right)\mathrm{d}\varphi &= \frac{1}{2}\left[\frac{\sin\left(\left(n+n'\right)2\pi\right)}{\left(n+n'\right)2\pi} + \frac{\sin\left(\left(n-n'\right)2\pi\right)}{\left(n-n'\right)2\pi}\right] \\ &= \begin{cases} 1, & n = n' = 0, \\ 1/2, & n = n' \neq 0, \\ 0, & n \neq n', \end{cases} = \delta_{n,n'}/\delta_n, \end{aligned} \tag{A.1}$$

and for $n = 1, 2, 3, \ldots$, $n' = 1, 2, 3, \ldots$ from the orthogonality of sine functions

$$\begin{aligned}\frac{1}{2\pi}\int_0^{2\pi} \sin(n\varphi)\sin\left(n'\varphi\right)\mathrm{d}\varphi &= \frac{1}{2}\left[\frac{\sin\left(\left(n-n'\right)2\pi\right)}{\left(n-n'\right)2\pi} - \frac{\sin\left(\left(n+n'\right)2\pi\right)}{\left(n+n'\right)2\pi}\right] \\ &= \begin{cases} 1/2, & n = n', \\ 0, & n \neq n', \end{cases} = \delta_{n,n'}/2, \end{aligned} \tag{A.2}$$

with the Kronecker symbol $\delta_{n,m} = 0$, $n \neq m$; $\delta_{n,m} = 1$, $n = m$ and the Heaviside symbol $\delta_{n=0} = 1$, $\delta_{n\neq 0} = 2$.

Special attention has to be given to the interior zone, where φ is limited to the interval $[-\varphi_0, \varphi_0]$. Orthogonality has therefore to be shown in this interval instead of the whole orbit around the cylinder $[0, 2\pi]$. But because the factor N scales the integral back to a whole orbit $N\varphi = \frac{\pi}{\varphi_0}\varphi$, the given orthogonality relations still hold with $\nu\varphi_0 = \eta\pi$, $\nu'\varphi_0 = \eta'\pi$:

$$\begin{aligned}\frac{1}{2\varphi_0}\int_{-\varphi_0}^{\varphi_0}\cos(\nu\varphi)\cos(\nu'\varphi)\,\mathrm{d}\varphi &= \frac{1}{2}\left[\frac{\sin\left(\left(\nu+\nu'\right)2\varphi_0\right)}{\left(\nu+\nu'\right)2\varphi_0}+\frac{\sin\left(\left(\nu-\nu'\right)2\varphi_0\right)}{\left(\nu-\nu'\right)2\varphi_0}\right]\\ &= \frac{1}{2}\left[\frac{\sin\left(\left(\eta+\eta'\right)2\pi\right)}{\left(\eta+\eta'\right)2\pi}+\frac{\sin\left(\left(\eta-\eta'\right)2\pi\right)}{\left(\eta-\eta'\right)2\pi}\right]\\ &= \begin{cases}1, & \eta=\eta'=0,\\ 1/2, & \eta=\eta'\neq 0,\\ 0, & \eta\neq\eta',\end{cases} \quad = \delta_{\eta,\eta'}/\delta_\eta,\end{aligned} \tag{A.3}$$

and with $\nu\varphi_0 = \left(\eta+\frac{1}{2}\right)\pi$, $\nu'\varphi_0 = \left(\eta'+\frac{1}{2}\right)\pi$:

$$\begin{aligned}\frac{1}{2\varphi_0}\int_{-\varphi_0}^{\varphi_0}\sin(\nu\varphi)\sin(\nu'\varphi)\,\mathrm{d}\varphi &= \frac{1}{2}\left[\frac{\sin\left(\left(\nu-\nu'\right)2\varphi_0\right)}{\left(\nu-\nu'\right)2\varphi_0}-\frac{\sin\left(\left(\nu+\nu'\right)2\varphi_0\right)}{\left(\nu+\nu'\right)2\varphi_0}\right]\\ &= \frac{1}{2}\left[\frac{\sin\left(\left(\eta-\eta'\right)2\pi\right)}{\left(\eta-\eta'\right)2\pi}-\frac{\sin\left(\left(\eta+\eta'+1\right)2\pi\right)}{\left(\eta+\eta'+1\right)2\pi}\right]\\ &= \begin{cases}1/2, & \eta=\eta',\\ 0, & \eta\neq\eta',\end{cases} \quad = \delta_{\eta,\eta'}/2.\end{aligned} \tag{A.4}$$

Appendix B. Mode coupling integrals

The integrals from Eq. 34, 43, 35 and 44 can be calculated analytically. The integrals from Eq. 34 and 43 have the values:

$$\begin{aligned}I^{\sin}_{x,y} =& \frac{1}{2\varphi_0}\int_{-\varphi_0}^{\varphi_0}\sin(x\varphi)\sin(y\varphi)\,\mathrm{d}\varphi\\ =& \frac{1}{2}\left[\frac{\sin\left((x-y)\,\varphi_0\right)}{(x-y)\,\varphi_0}-\frac{\sin\left((x+y)\,\varphi_0\right)}{(x+y)\,\varphi_0}\right]\\ \xrightarrow[x=y=0]{}& 0;\\ \xrightarrow[x=y\neq 0]{}& \frac{1}{2}\left[1-\frac{\sin\left(2x\varphi_0\right)}{2x\varphi_0}\right].\end{aligned} \tag{B.1}$$

The integrals from Eq. 35 and 44 have the values:

$$\begin{aligned}I^{\cos}_{x,y} =& \frac{1}{2\varphi_0}\int_{-\varphi_0}^{\varphi_0}\cos(x\varphi)\cos(y\varphi)\,\mathrm{d}\varphi\\ =& \frac{1}{2}\left[\frac{\sin\left((x+y)\,\varphi_0\right)}{(x+y)\,\varphi_0}+\frac{\sin\left((x-y)\,\varphi_0\right)}{(x-y)\,\varphi_0}\right]\\ \xrightarrow[x=y=0]{}& 1;\\ \xrightarrow[x=y\neq 0]{}& \frac{1}{2}\left[1+\frac{\sin\left(2x\varphi_0\right)}{2x\varphi_0}\right].\end{aligned} \tag{B.2}$$

References

Abramowitz, M., Stegun, I. A., 1964. Handbook of Mathematical Functions: With Formulas, Graphs, and Mathematical Tables. Courier Corporation. 5

Beranek, L. L., Mellow, T. J., 2012. Acoustics: Sound Fields and Transducers. Academic Press, Amsterdam. 2, 4

Cambel, V., Tóbik, J., Šoltýs, J., Fedor, J., Precner, M., Gaži, Š., Karapetrov, G., 2013. The influence of shape anisotropy on vortex nucleation in Pacman-like nanomagnets. Journal of Magnetism and Magnetic Materials 336, 29–36. 2

Cavicchi, T. J., O'Brien, W. D., 1988. Acoustic scattering of an incident cylindrical wave by an infinite circular cylinder. IEEE Transactions on Ultrasonics, Ferroelectrics, and Frequency Control 35 (1), 78–80. 5

Duhamel, D., Nov. 1996. Efficient calculation of the three-dimensional sound pressure field around a noise barrier. Journal of Sound and Vibration 197 (5), 547–571. 1, 20

Flax, L., Varadan, V. K., Varadan, V. V., 1980. Scattering of an obliquely incident acoustic wave by an infinite cylinder. The Journal of the Acoustical Society of America 68 (6), 1832–1835. 7

Hornikx, M., Kaltenbacher, M., Marburg, S., 2015. A Platform for Benchmark Cases in Computational Acoustics. Acta Acustica united with Acustica 101 (4), 811–820. 1

Howett, C. J. A., Spencer, J. R., Hurford, T., Verbiscer, A., Segura, M., 2012. PacMan returns: An electron-generated thermal anomaly on Tethys. Icarus 221 (2), 1084–1088. 2

Kasess, C. H., Kreuzer, W., Waubke, H., 2016. An efficient quadrature for 2.5D boundary element calculations. Journal of Sound and Vibration 382, 213–226. 1, 20

Le Bars, M., Worster, M. G., 2006. Solidification of a binary alloy: Finite-element, single-domain simulation and new benchmark solutions. Journal of Computational Physics 216 (1), 247–263. 1

Loguidice, B., Barton, M., 2009. 13 - Pac-Man (1980): Japanese Gumption, American Consumption. In: Vintage Games. Focal Press, Boston, pp. 179–193. 2

Marburg, S., 2002. Six boundary elements per wavelength: Is that enough? Journal of Computational Acoustics 10 (01), 25–51. 1

Mechel, F. P., 2005. The Cat's Eye Model. Acta Acustica united with Acustica 91 (4), 653–660. 1, 4, 7

Melissinos, C., Broun, E., Mika, M., 2012. The Art of Video Games: From Pac-Man to Mass Effect. Welcome Books, New York. 2

Morris, P. J., 1995. The scattering of sound from a spatially distributed axisymmetric cylindrical source by a circular cylinder. The Journal of the Acoustical Society of America 97 (5), 2651–2656. 2, 6

Sherer, S. E., 2004. Scattering of sound from axisymetric sources by multiple circular cylinders. The Journal of the Acoustical Society of America 115 (2), 488–496. 6

Simpson, M. J., Landman, K. A., 2007. Nonmonotone chemotactic invasion: High-resolution simulations, phase plane analysis and new benchmark problems. Journal of Computational Physics 225 (1), 6–12. 1

Tam, C. K. W., Hardin, J. C., 1997. Second Computational Aeroacoustics (CAA) Workshop on Benchmark Problems. 1

Williams, E. G., 1999. Fourier Acoustics. Academic Press, London. 4

Ziegelwanger, H., Majdak, P., Kreuzer, W., 2015. Mesh2HRTF: Open-source software package for the numerical calculation of head-related transfer functions. In: Proceedings of the 22nd International Congress on Sound and Vibration. Florence, IT. 1